Check for updates

A novel test device and quantitative colorimetric method for the detection of human chorionic gonadotropin (hCG) based on Au@Zn–salen MOF for POCT applications†

Reda M. Mohamed,*[a] Said M. El-Sheikh, [iD] *[b] Mohammad W. Kadi,[a] Ammar A. Labib[c] and Sheta M. Sheta [iD] *[c]

The human chorionic gonadotropin (hCG) hormone is a biomarker that can predict tumors and early pregnancy; however, it is challenging to develop sensitive qualitative-quantitative procedures that are also effective, inventive, and unique. In this study, we used a novel easy *in situ* reaction of an organic nano-linker with $Zn(NO_3)_2 \cdot 6H_2O$ and $HAuCl_4 \cdot 3H_2O$ to produce a gold–zinc–salen metal–organic framework composite known as Au–Zn–Sln-MOF. A wide variety of micro-analytical instruments and spectroscopic techniques were used in order to characterize the newly synthesized Au–Zn–Sln-MOF composite. Disclosure is provided for a novel swab test instrument and a straightforward colorimetric approach for detecting hCG hormone based on an Au–Zn–Sln-MOF composite. Both of these methods are easy. In order to validate a natural enzyme-free immunoassay, an Au–Zn–Sln-MOF composite was utilized in the role of an enzyme; a woman can use this gadget to determine whether or not she is pregnant in the early stages of the pregnancy or whether or not her hCG levels are excessively high, which is a symptom that she may have a tumor. This cotton swab test device is compatible with testing of various biological fluids, such as serum, plasma, or urine, and it can be easily transferred to the market to commercialize it as a costless kit, which will be 20–30% cheaper than what is available on the market. Additionally, it can be used easily at home and for near-patient testing (applications of point-of-care testing (POCT)).

Introduction

Point-of-care testing (POCT) is now widely used in the healthcare, medical, and clinical professions for early illness monitoring and rapid commercial diagnostic instruments.[1–3] Illness screening and treatment options rely heavily on early detection of disease and tumour biomarkers and rapid diagnosis.[4] In many instances, patients need immediate results from diagnostic tests performed in medical laboratories, even though these tests often take a long time, necessitate multiple stages of preparation for the sample, and call for sophisticated tools for infrastructural construction and staff with extensive training.[5,6] In countries with few medical resources, POCT has emerged to be an invaluable tool for both patients and their doctors. For example, various benefits of POCT have led to annual sales of more than three and a half million euros in Europe. Self-testing devices (an instrument the user operates on their own)/(POCT) have been expanding at a rapid rate in recent years, with roughly 10% larger market size than what it was a decade ago. Moreover, the demands for POCT in several industries, such as genetic testing, pharmacology, and healthcare, are potential growth areas, expanding the purpose and offering a future vision for ongoing development and encouraging novel ideas in this crucial industry.[7]

The human chorionic gonadotropin (hCG) polypeptide hormone is a 37 000 Dalton multi-functional heterodimeric glycoprotein that results from placental development trophoblast cells during pregnancy and it is upregulated in trophoblast and non-fibroblast tumours.[8–10] It is generally made up of two subunits (α-hCG and β-hCG). However, it can undergo glycosylation at eight different locations, which results in it having a wide variety of glycol forms. Quantitative and qualitative hCG tests are typically performed to determine a woman's pregnancy status.[11] Rapid hCG testing can be performed using qualitative methods on urine or serum samples at a point-of-care testing centre (POCT). However, serum quantitative hCG testing is usually performed in a clinical setting.

[a]*Chemistry Department, Faculty of Science, King Abdul-Aziz University, P.O. Box 80203, Jeddah, 21589, Saudi Arabia. E-mail: redama123@yahoo.com*

[b]*Department of Nanomaterials and Nanotechnology, Central Metallurgical R & D Institute, Cairo, 11421, Egypt. E-mail: selsheikh2001@gmail.com*

[c]*Department of Inorganic Chemistry, National Research Centre, Cairo, 12622, Egypt. E-mail: dr.sheta.nrc@gmail.com; Tel: +201009697356*

† Electronic supplementary information (ESI) available. See DOI: https://doi.org/10.1039/d2ra07854f

Pregnancy is considered negative when the hCG titer is less than 5.0 mIU mL^{-1}, equivocal when the titer is between 5.0 and 20.0 mIU mL^{-1}, and positive when the titer is greater than 25.0 mIU mL^{-1} in the quantitative assay.[12,13] Numerous biochemical and biological processes rely on hCG. Not only does it serve as a pregnancy test, but also it has many other clinical uses that have been revealed. Women and men with a trophoblastic placental tumour have abnormally high hCG levels.[14] High hCG hormone levels in nonpregnant women are not indicative of ovarian, pancreatic, bladder, pulmonary, gastrointestinal, or hepatic tumours.[15]

The increased hCG concentration can be used for the diagnosis of the disease of gestational trophoblastic, as well the tumours of testicular germ cells (testicular cancers).[14,16] Besides the diagnosis of ectopic pregnancies in females and a variety of neoplasm tumours incorporated into a more significant screening for fetal aneuploidy together with other indicators.[8] A crucial role of the hCG hormone during pregnancy is to stimulate uterine angiogenesis, ensuring that the invasive placenta receives the maximum blood supply possible.[8,16] It acts as an enhancer of pituitary LH throughout the reproductive phase of female mammals and is a cancer promoter in all human malignancies.[17,18] Research on the efficient, accurate, and sensitive detection of hCG hormone in plasma, serum, or urine samples is essential for ongoing advancement.[19-26] All electrochem-volta-luminescence assay[8,12,27] and fluorescence methods[28] are just some of the analytical techniques, spectroscopic, methods, and special devices that report hCG detection methods. It is common knowledge that each aforementioned approaches have both positive and negative qualities. Therefore, experts from all over the world are interested in the constant development of new approaches. One of the most popular techniques, colloidal–gold immune chromatography can be used to identify and screen for a wide variety of biomarkers quickly and at a low cost.[20] This technique integrated the aspects of chromatography and immunoassay instruments. Antibodies are the primary building blocks of these immunosensors, and their production and improvement hinge on immobilization and signal amplification.[29,30]

In contrast, metal–organic frameworks (MOFs) are intriguing classes of high-porosity crystals and heterogeneous materials with pores and channels of variable sizes that can capture and absorb, for instance, tiny molecules and gases.[31-33] They are synthesized from the reaction of inorganic nodes (clusters or metal nodes) with organic linkers by forming noncovalent and covalent bonding.[34,35] These materials (MOFs) can have different topologies, and morphologies. As well as, can be functionalized, regulated, and modified easily by a selection matrix of various clusters, and metals, with a matrix of diverse organic ligands/linkers.[36,37] Some of the many different types of production of MOFs as functional materials have been accelerated through encapsulation or embedding of nanoparticles of noble metals such as Au, Pt,[38,39] and salen MOFs.[40-45] The binding of substrates leads to the formation of multi-metallic salen frameworks whereby metal hosts generate adducting complexes with enhanced structural ordering.[46-49] These materials are currently receiving a lot of attention because of the many different ways in which they can be used, as well as their excellent thermal and chemical stability, high surface area, and manageable pore size.[50-59]

This work involved the synthesis of a novel gold–zinc–salen-based-MOF (Au–Zn–Sln-MOF) composite by reacting $Zn(NO_3)_2 \cdot 6H_2O$ and $HAuCl_4 \cdot 3H_2O$ at a molar ratio of 1 : 1 utilizing an organic nano linker previously prepared by Sheta et al.[60] Microanalytical and spectral methods such HR-TEM, FE-SEM, EDX, XRD, elemental analysis, FT-IR, UV-vis, and TGA/DSC were used to characterize the synthetic Au–Zn–Sln-MOF composite. The current research went further by using the Au–Zn–Sln-MOF composite as a promising biosensor for detecting and quantifying hCG hormone at ultra-low concentrations, using both strip devices for qualitative detection and a colorimetric approach for quantification, both of which yielded statistically validated acceptable results. Besides thoroughly investigating the interaction mechanism, this study compared and contrasted published qualitative and quantitative approaches.

Results and discussion

Characterization of Au–Zn–Sln-MOF composite, Au–Zn–Sln-MOF@Ab, and Au–Zn–Sln-MOF@Ab@hCG

Au–Zn–Sln-MOF composite was synthesized via a simple in situ reaction organic nano-linker containing an identical molar ratio of $Zn(NO_3)_2 \cdot 6H_2O$ and $HAuCl_4 \cdot 3H_2O$. The mechanism of this reaction consists of four stages: first, Au is reduced using DMF and ethanol,[61-63] where DMF was recently introduced as a reducing agent by Marzán. Since DMF is a strong reducing agent, it has been used to synthesize nanoparticles of Ag^+,[64,65] Ni^{2+}/Co^{2+},[66] Cu^{2+},[67] Pd^{2+},[68] and Au^{3+} ions,[69,70] at room temperature, using the eqn (1):

$$3HCONMe_2 + 2AuCl_4^- + 3H_2O = 2Au^0 + 3Me_2NCOOH-8Cl^- + 6H^+ \tag{1}$$
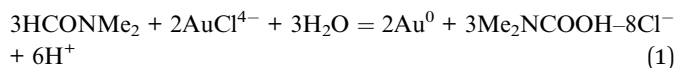
In the second stage, the helical complex is formed by placing Zn(II) ions in the middle of the nano-linker. In the third stage, Au is incorporated into Zn(II)–salen MOF by forming an adduct complex; and in the fourth stage, gold ion binds to the substrate at the complex's outer node leading to a higher degree of structural order and the formation of a the Au–Zn(II)–Sln-MOF composite.

The percentage of precipitate production from the reaction was 66.3%. Several quantitative and qualitative microanalytical methods were used to examine and characterize in depth to clarify the proposed structure.

SEM, EDX, and TEM spectroscopy

The typical morphological characteristics of the Au–Zn–Sln-MOF composite are illustrated in FE-SEM images (Fig. 1A–E). In Fig. 1A–C, it is seen that smooth nano-spherical surfaces of Au and Zn–Sln-MOF are wrapped in a layer of nanosheets. The Zn–Sln-MOF nanosheet thickness is less than 100 nm. In contrast, the nano-spherical structure of Au is a strong aggregate of a single size particle found throughout the matrix, as seen in an enlarged FE-SEM image, with a diameter of roughly
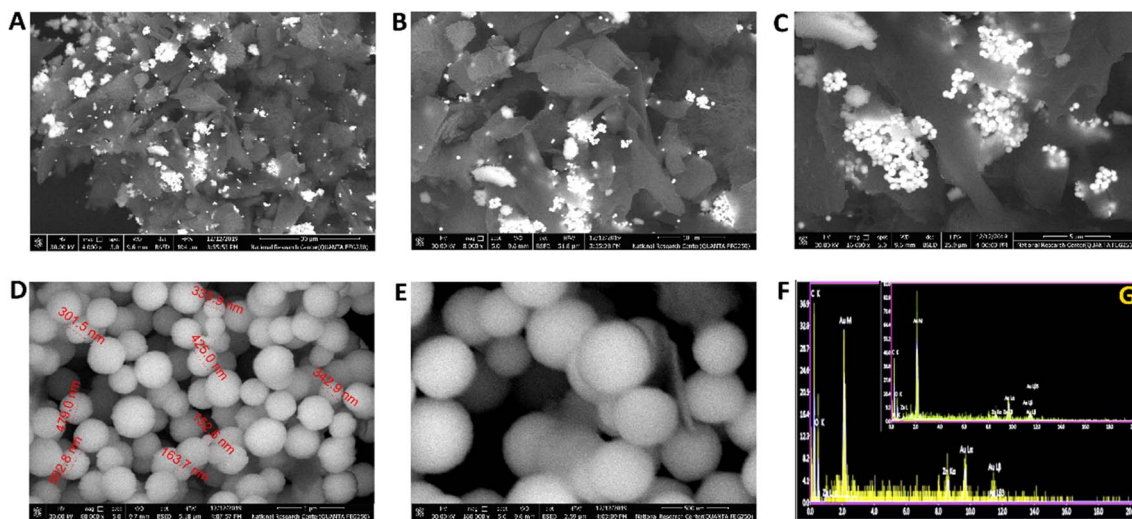
Fig. 1 (A–E) The FE-SEM images at a different magnification of the Au–Zn–Sln-MOF composite, and (F and G) EDX analysis at a different point of Au–Zn–Sln-MOF composite.

350–450 nm (Fig. 1D and E). In addition, Zn, Au, carbon, nitrogen, and oxygen were identified as constituents of the Au–Zn–Sln-MOF composite using EDX mapping analysis (Fig. 1F and G, insert-in F, and Table S1†). Moreover, the cross-section revealed by mapping EDX analysis and the exceptional distribution of the aforementioned MOF elements both corroborated the development of the Au–Zn–Sln-MOF composite (Fig. 1F and G).

Fig. 2A–C displays TEM images of the Au–Zn–Sln-MOF composite. These findings are consistent with FE-SEM and show that spherical Au nanoparticles (with a size of around 350–450 nm) have a higher contrast than the other shapes. Small nanosheets of Zn–Sln-MOF are also produced in the region of interest. The crystalline structure of gold nanoparticles was verified by analyzing the diffraction pattern of a single sphere

Fig. 2 (A–C) The Au–Zn–Sln-MOF TEM images at various magnification, (D) the selected area diffraction patterns of the Au–Zn–Sln-MOF.

(Fig. 2D), whereas the rings allocated to the (111), (200), and (220) planes of gold's FCC crystalline lattice demonstrated the polycrystalline nature of Zn–Sln–MOF nanosheets.

FE-SEM pictures of the Au–Zn–Sln-MOF composite on the swab's surface are shown in Fig. 3A–D at varying magnifications. These pictures show that the Au–Zn–Sln-MOF composite is evenly dispersed on the swab's exterior (Fig. 3A and B illustrate the good distribution). Although a robust relationship and association between Au and swab are shown in Fig. 3C and D. TEM pictures of Au–Zn–Sln-MOF@Ab on swab fibers without hCG hormone (Fig. 3E and F) and with the hCG hormone (Fig. 3G and H) are shown in the following figures. In Fig. 3E and F, surface nanosheets of an Au–Zn–Sln-MOF composite appeared. On the other hand, the swab's surface adhesion strength is confirmed in which Ab forms a network around Au nanoparticles, Zn–Sln–MOF nanosheets, and the swab (Fig. 3G and H, various magnifications).
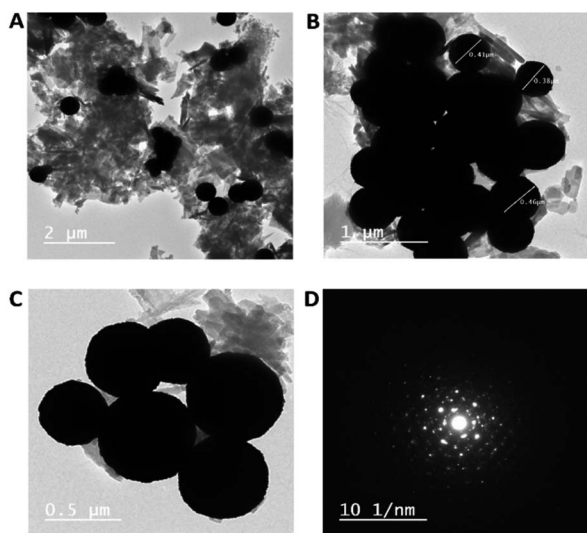
UV-vis spectra

Electronic reflection and bandgap spectra of the Au–Zn–Sln-MOF composite *vs.* the organic linker are shown in Fig. 4A and B, respectively. As can be seen in Fig. 4A, the Au–Zn–Sln-MOF composite exhibits a considerable blueshift in its reflection peaks relative to the organic linker, with peaks appearing at 228, 278, 373, and 626 nm. As a result of the enhanced conjugation between the organic linker leading to a rise in the HOMO valence band energy, the energy bandgap of the Au–Zn–Sln-MOF composite was reduced to (1.60 and 1.75 eV), as shown in (Fig. 4B). In addition, gold nanoparticle surface plasmon resonance was linked to the observation of a broad absorption band with a center wavelength of 465 nm.[38]

FT-IR

A comparison of the FT-IR spectrum of the Au–Zn–Sln-MOF composite and previously reported[38,71,72] Zn-MOF spectra is shown in (Fig. 4C). The (NH$_2$) peak is located at 3281 cm^{-1} in
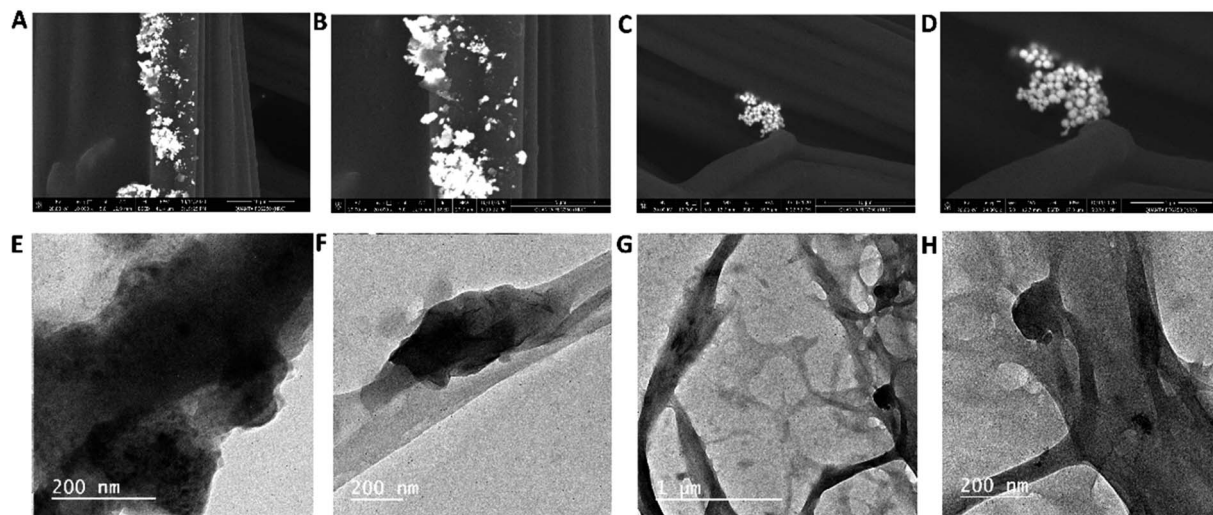
Fig. 3 (A–D) The Au–Zn–Sln-MOF@Ab on the surface of swab FE-SEM images at a different magnification, (E–H) TEM images at different magnification of the Au–Zn–Sln-MOF@Ab on the surface of swab fibers [(E) without and (F–H) with h-CG hormone.
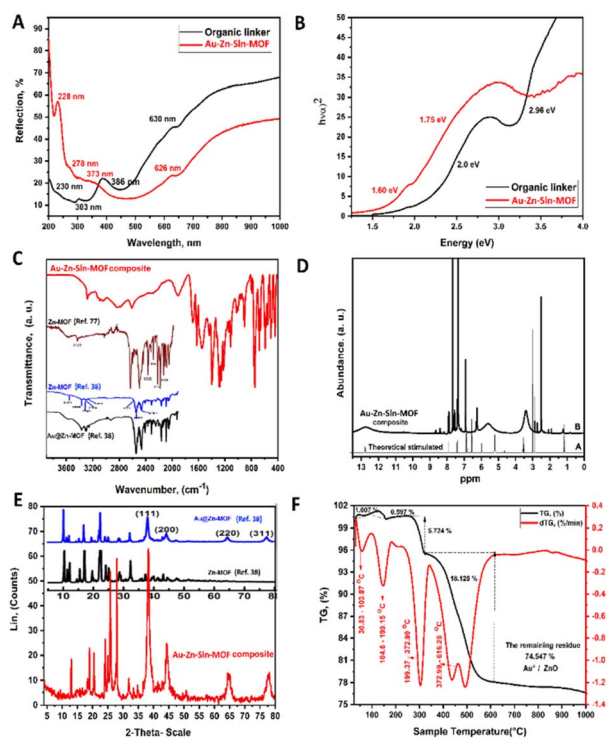

Fig. 4 (A) UV-Vis spectra of Au–Zn–Sln-MOF composite and organic linkers, (B) energy bandgap of Au–Zn–Sln-MOF and organic linker, (C) Au–Zn–Sln-MOF FT-IR spectrum, (D) the Au–Zn–Sln-MOF ^{1}H-NMR, (E) Au–Zn–Sln-MOF XRD spectra, (F) TGA–DTA graph of the Au–Zn–Sln-MOF composite.

the spectra and the aromatic ν(C–H) peak is located at around 3060 cm^{-1}.[38,71] The 1680 cm^{-1}, 1626 cm^{-1}, and 1550 cm^{-1} bands correspond to the equivalent stretches of ν(C=O), ν(C=N), and ν(NH), respectively.[38,71] The as-symmetric stretching of ν(O–C–O) groups are responsible for the strong peaks located at

1437 cm^{-1} and the peak at 1397 cm^{-1} is attributed to ν(C=C).[38,73–75] The d(C–H) and g(C–H) vibrations of the aromatic benzene ring (ν(CH)) are attributed to the bands at 1145 and 796 cm^{-1}, respectively.[73] The peaks at 749–662 cm^{-1} are attributed to in- and out-of-plane aromatic ring bending vibrations.[38] Zinc ion complexation with the organic linker is indicated by the appearance of bands at 507 and 443 cm^{-1}, which are attributed to coordination and covalent with oxygen and nitrogen (ν(Zn < –O)), (ν(Zn–N)), respectively (Fig. S3†).[76]

^{1}H-NMR spectra

A comparison of the theoretically predicted and experimentally observed ^{1}H-NMR spectra of the Au–Zn–Sln-MOF composite is shown in (Fig. 4D). The OH of the carboxylic group node showed up as a signal at 12.65 ppm in the spectrum. All signals between 7.93 and 6.7 ppm have been attributed to protons in aromatic rings. The amine groups account for the wide 5.5 ppm signal, while the 8.13 and 2.9 ppm signals are attributed to the CHO and CH$_3$ of the DMF solvent, respectively. Ethanol's CH$_2$ and CH$_3$ protons are responsible for the 3.5 and 1.22 ppm, peaks, respectively.[53]

XRD analysis

Fig. 4E illustrates the XRD patterns of the powdered Au–Zn–Sln-MOF composite, in comparison with the previous studies on Zn-MOF.[38,71,72,77,78] Sharp peaks in the XRD patterns of the Au–Zn–Sln-MOF composite indicate that the crystalline phase of the composite was successfully obtained. In addition, the diffraction patterns coincided with those reported for Zn-MOF-JCPDS no. 18-1486.[71] The XRD patterns of the Au–Zn–Sln-MOF composite clearly showed recognizable planes of face-centered cubic gold nanoparticles (111), (200), (220), and (311), which may be identified from the presence of the diffraction peaks at 38.29, 44.46, 64.66, and 77.67.[38,39]

Thermal analysis

Graphs of thermal expansion and contraction (TGA/DTG) (Fig. 4F) were used to evaluate the thermal properties of the Au–Zn–Sln-MOF composite and to compare them with previous studies of Zn-MOF.[71,77] The composite thermogram of the Au–Zn–Sln-MOF revealed four distinct step points. The first break in weight loss, 1.005 wt% between 30.83 and 103.87 °C, may be attributable to free-lattice ethyl alcohol molecules. At temperatures between 104.6 and 199.15 °C the second weight loss took place, which was the loss of inter-lattice water molecules, which may account for the remaining weight loss (0.597 wt%). A possible explanation for the third weight loss value (5.724% wt%) between 199.37 and 372.99 °C is the evaporation of free-lattice DMF molecules. The decomposition of the organic groups inside the framework may account for the final point of weight loss (18.125 wt%) at temperatures between 372.99 and 616.28 °C. The chemical stability of the Au–Zn–Sln-MOF composite was demonstrated by its resistance to degradation from 372.99 to 616.28 °C. After subjecting the composite to heat over 997.45 °C, 74.547 wt% of its original mass remained. X-ray diffraction patterns identified crystallinity phases associated with Au metal and ZnO.[71,77]

The determination of the hCG hormone: applications and the validation of methods

Detection of the hCG hormone qualitatively using a swab test instrument and subsequent confirmation. The experimental section explains how the detection probe (Au–Zn–Sln-MOF@Ab) was made using the information from the literature as a guide, with a few tweaks.[20,24,79–81] Cotton swabs were then soaked in the detecting probe for an entire night after the preparatory stage, as depicted in (Fig. 5A). Since the swabs were allowed to dry at room temperature, the swab test is now operational (Fig. 5B).

The following procedures were followed during detection and verification: after sitting out at room temperature for about ten minutes, each swab was submerged for one minute in a vial containing a varied concentration of the hCG-hormone standard (5, 20, 50, 100, 500, 1000 mIU mL^{-1}) (Fig. 5C). Swab (a) represents the control; swab (b) represents 5.0 mIU mL^{-1}; swab (d) represents 50.0 mIU mL^{-1}; swab (e) represents 100.0 mIU mL^{-1}; swab (f) represents 500.0 mIU mL^{-1}; and swab (g) represents 1000.0 mIU mL^{-1}, as illustrated in Fig. 5C. The figure shows that at a concentration of over 20.0 mIU mL^{-1}, the swab color changed immediately to green after 10 minutes (Fig. 5C(c) and (g)). Further, the swab test can be classified as the detection of the hCG hormone qualitatively using a swab and subsequent confirmation (positive pregnant samples hCG concentration ≥ 20 mIU mL^{-1}) since the intensity of the green color is directly proportionate to the hCG concentration. In contrast, no color shift is seen in the case of an hCG concentration of 5.0 mIU mL^{-1} (Fig. 5C(b)), indicating that this sample is negative for pregnancy (negative pregnancy samples have an hCG value ≤ 5.0 mIU mL^{-1}). The swab test tool's biosensing technique relies on the necked eye color change to green caused by sandwich immunocomplexes formed between the antigen and antibody
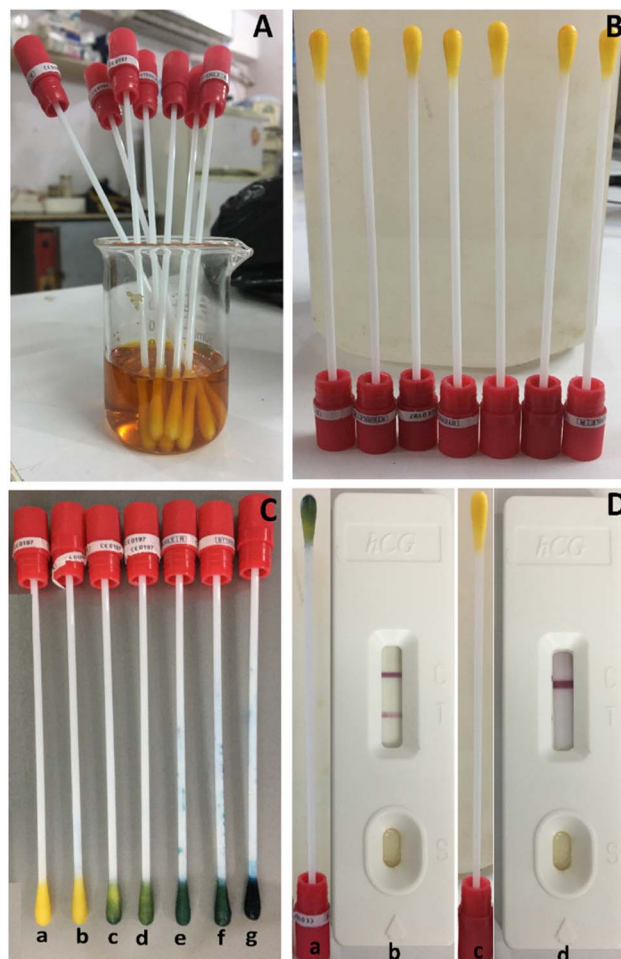

Fig. 5 A smartphone photos images for preparation and optimization of the swab test device: (A) a sterile cotton swabs soaked in a solution of Au–Zn–Sln-MOF@Ab, (B) ready to used test swab device, (C) a swabs test-based device optimization against different β-hCG hormone concentrations standard (mIU mL^{-1}) [(a) control; (b) 5.0; (c) 20.0; (d) 50.0; (e) 100.0; (f) 500.0; and (g) 1000.0], and (D) a comparison of the performance of the swab test-based device with pregnancy cassette in market [(a) and (b) pregnant case are positive; (c) and (d) pregnant cases are negative].

on the surface of the gold nanoparticles of the Zn–Sln-MOF composite.

The feasibility of using the current swab test on genuine samples was studied. Two commercial pregnancy hCG cassette fast test kits, the "NOVA®"[82] and the "Medical-Disposables.us®"[83] were used to evaluate and compare the results of 150 true negative and positive pregnancy samples (50 urine, 50 plasma, and 50 serum samples) swabbed with the present swap. Fig. 5D displays some of the outcomes that were found. Figures (a) and (b) in Fig. 5D depict a positive pregnancy case using the pregnancy cassette and the most up-to-date swab testing equipment available on the market, while, Fig. 5D(c) and (d) depict a negative pregnancy case using the same devices. In general, the results show that the swab test equipment is quite sensitive with both samples that are considered positive and samples that are considered negative in a variety of biological

samples. Two commercially available products[82,83] were used to check the results, and Table S2 of the ESI† has a summary of how the data were evaluated. Based on the results in the table, the efficiency of the present swab test is 96.2 percent, which is higher than that of the two existing products.

Additionally, the durability and selectivity of the swab test instrument were studied. First, the sensitivity and specificity of the swab test device were determined by testing it with a panel consisting of various hormones, proteins, electrolytes, and organic matrices (Fig. 6A): [a] control; [b] 100 mIU mL^{-1} hCG; [c] 10 μg mL^{-1} bovine serum albumin (BSA); [d] 1000 ng mL^{-1} carcinogenicity-antigen (CEA); [e] 1000 ng mL^{-1} follicle-stimulating hormone (FSH); [f] 1000 ng mL^{-1} luteinizing hormone (LH); [j] 1000 ng mL^{-1} prolactin (PRL); [h] 1000 ng mL^{-1} prostate-specific-antigen (PSA); [i] 1000 ng mL^{-1} α-feto-protein (AFP); [j] 500 mg dL^{-1} glucose (Glu); [k] 100 mg dL^{-1} uric acid (UA); [l] 100 mM sodium ion (Na$^+$); [m] 100 mM chloride ion (Cl$^-$). As shown in Fig. 6A, additional evidence supports the color change to green in the hCG sample, while no change occurs in the case of other interfering substances when compared to the control swab, which demonstrates the outstanding selectivity for hCG. Additionally, the swab test lifetime was examined for six months, as shown in Fig. 6B. The results demonstrate that the swab testing apparatus is functioning at peak efficiency during this time, suggesting that the swabs' quality will be adequate for their intended use and conform to the standards set forth by the marking.

The accuracy and precision were also evaluated in intra- and inter-assays, as well as across its lifetime evaluation period, revealing excellent performance. Also, the cost of the present

swab test equipment is expected to decrease by at least 40% in the future compared to other devices in the market. Fig. 6C shows a smartphone photograph of a collection of swab test devices that are now available for sale. After being inserted into a plastic well, each swab can be used at home if necessary. All of this adds up to a promising, efficient, sensitive, selective, accurate, precise, low-cost, user-friendly technology that can be tested at home and that is compatible with a variety of biological fluids (plasma, serum, and urine).

Validation of a colorimetric assay for the quantitative detection of human chorionic gonadotropin. Fig. 7A shows the absorption spectra acquired at RT for the Au–Zn–Sln-MOF composite, Au–Zn–Sln-MOF@Ab, and Au–Zn–Sln-MOF@Ab@hCG. As can be seen in Fig. 7A, the UV-vis absorption spectra of the Au–Zn–Sln-MOF composite showed three distinct peaks at 328, 465, and 646 nm. Once antibodies have been attached to gold nanoparticles, it was found that the Au–Zn–Sln-MOF@Ab exhibited two UV-Vis absorption peaks at 318 and 448 nm, with the third band disappearing and a redshift of roughly 10 nm. There were three UV-Vis absorption peaks observed for the Au–Zn–Sln-MOF@Ab@hCG, at 321, 450, and 620 nm, respectively. A small blue shift of 2 to 3 nm was observed when analyzing the differences in the absorption spectra of Au–Zn–Sln-MOF@Ab and Au–Zn–Sln-MOF@Ab@hCG. The transition from a light brown to a green color coincided with the appearance of a new absorption peak at 620 nm. This blue shift may be explained by an increase in the hydration radius of the hCG hormone after the incorporation of gold nanoparticle coatings onto hCG suggesting the development of a sensitive sensing tool.[20,24,79,80]

The hCG detection and quantification capabilities of the Au–Zn–Sln-MOF@Ab colorimetric biosensor were investigated. Fig. 7B depicts the results of an investigation into the relationship between the absorption spectra of Au–Zn–Sln-MOF@Ab and varying concentrations of hCG. Absorption spectra bands are enhanced with blueshift of around 2–3 nm by appearing at 620 nm, as illustrated in Fig. 7B. The absorption intensities also increased steadily as the hCG concentration was raised from 0.001 mIU mL^{-1} to 3000.0 mIU mL^{-1}. In addition, as can be seen in Fig. 7C, Au–Zn–Sln-MOF@Ab solutions changed from a pale brown to a vibrant green. Therefore, Au–Zn–Sln-MOF@Ab can be employed as a colorimetric biosensor and as a naked-eye indication for the hCG hormone. As shown in Fig. 7D, when the experimental conditions were optimized, a linear dependence was observed between the absorbance intensities of the three peak areas and a series of standard hCG phosphate-buffered solutions (321, 450, and 620 nm). In the suggested colorimetric immunoassays, two distinct regions of hCG concentration were seen in the calibration curves, owing to the Hook effect, one at an absorption peak of 620 nm (Ab$_{620}$) with a range of 0.001 to 5.0 mIU mL^{-1} and another at 10.0 to 3000.0 mIU mL^{-1}. The fitted eqn (2) and (3) for the lower and higher concentration ranges (two regions), respectively, can express as:
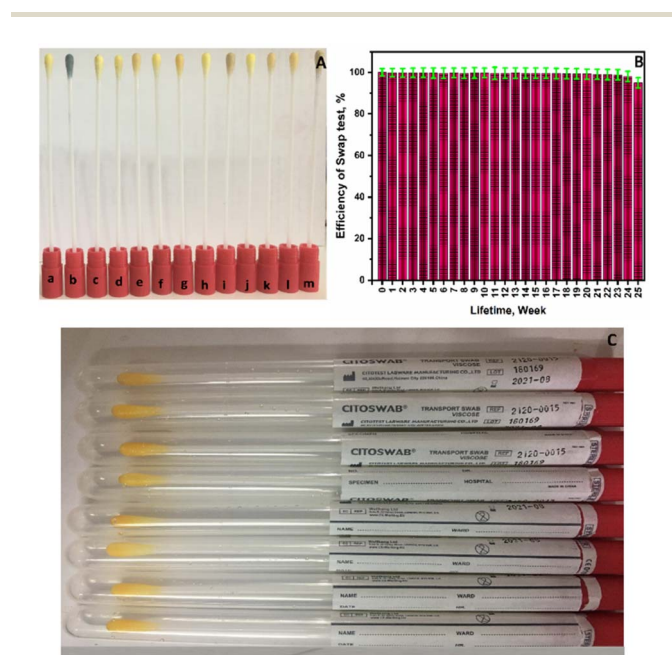

Fig. 6 (A) The selectivity evaluation for swab test-based device [control = a, β-hCG = b, BSA = c, CEA = d, FSH = e, LH = f, PRL = g, PSA = h, AFP = I, Glu = j, UA = k, Na$^+$ = l, Cl$^-$ = m] (B) the lifetime (week) evaluation of swab test-based device, and (C) a smartphone photo image for ready to used swab test-based device for marketing.
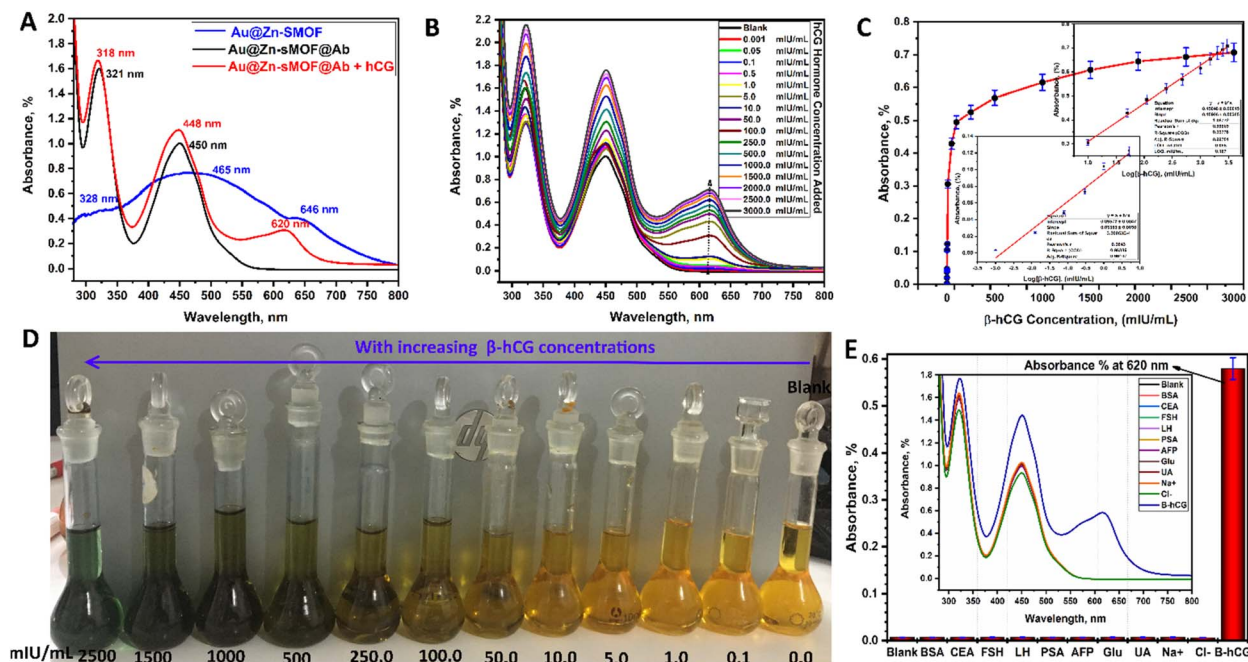
$$\text{Absorbance intensity (Abs}_{620}) = 0.150 + 0.159 \log[\text{hCG}]$$
$$\text{with } r^2 = 0.998, \qquad (2)$$

Fig. 7 (A) UV-Vis spectra the Au−Zn−Sln-MOF composite, Au−Zn−Sln-MOF@Ab, and Au−Zn−Sln-MOF@Ab@β-hCG, (B) UV-Vis response behavior spectra of Au−Zn−Sln-MOF@Ab composite against hCG hormone at different concentrations, (C) A dependence calibration graph of the proposed colorimetric immunoassays against hCG at different concentrations [insert in: a calibration graphs at two regions of concentrations between Abs-intensity and log[β-hCG]], (D) A smartphone photo for the Au−Zn−Sln-MOF composite color change by the increasing of the concentration of β-hCG, and (E) A histogram of evaluation of selectivity of the Au−Zn−Sln-MOF@Ab [insert in: the Au−Zn−Sln-MOF@Ab absorption intensities towards β-hCG hormone and selected different interfering analytes].

$$\text{Absorbance intensity (Abs}_{620}) = 0.096 + 0.034 \log[\text{hCG}]$$
$$\text{with } r^2 = 0.991, \tag{3}$$

With lower limits of detection and quantification (LOD = 0.055 mIU mL^{-1} and LOQ = 0.167 mIU mL^{-1}), the colorimetric immunoassay approach based on Au−Zn−Sln-MOF@Ab showed outstanding sensitivity for hCG detection. Tables S3 and S4† provide the results of a summary analysis of the data from the comparisons and the regression equations, respectively.[5,8,9,12,19,20,26,27] The purpose of this study is to determine the potential sensitivity and selectivity of Au−Zn−Sln-MOF@Ab towards hCG using current colorimetric immunoassay techniques, such as in swab test selectivity evolution. Fig. 7E compares the Au−Zn−Sln-MOF@Ab absorption spectrum to that of a variety of typical interferences, including BSA, CEA, FSH, LH, PSA, AFP, Glu, UA, Na$^+$, and Cl$^-$. This histogram (inserted into the absorption spectra) demonstrates that hCG significantly amplifies the results of the Abs$_{620}$ intensity, whilst the other interfering matrix does not. The results among which demonstrated the high selectivity of the Au−Zn−Sln-MOF@Ab for hCG.

Each concentration of hCG (1.0, 10.0, 100.0, 500.0, and 1500.0 mIU mL^{-1}) was measured three times to determine the inter- and intra-day accuracy and precision of the current colorimetric immunoassay approach. Abs$_{620}$ intensity histograms for the intervals between days and the days themselves, as well as a statistical analysis of the data, can be found in Fig. S4 and S5,† respectively, and Table S5.† The results have

been summarized and examined, showing that the current work is accurate, precise, reducible, and repeatable.

Further analysis of the proposed colorimetric immune-accuracy biosensors in assessing the hCG concentration content in a variety of actual samples (serum, plasma, and urine samples), as well as to study the practicality of using the sensor in clinical applications was performed. The evaluation was performed by adding hormones at varying quantities (0.5, 10.0, 100.0, and 1000.0 mIU mL^{-1}) to a variety of genuine samples and determining the percentage of hormone that was recovered. Table S6† is a representation of the results that were obtained. According to the statistics in the table, the percentage of samples that were collected ranged anywhere between 98.84% to 100.50% for serum samples 96.6% to 99.44% for plasma samples and 96.1% to 97.48 for urine samples. These results demonstrate that the approach that was presented is adaptable, sensitive, and effective for the quantification of hCG in a variety of genuine samples and that this method will be a promising future analytical tool for the simple and rapid detection and quantification of hCG.

Mechanism of biosensing

The following strategies comprise the basis for studying the biosensing mechanism and the features of hCG hormone trapping. The basic physicochemical features of the analytes and the creation of immunocomplexes in a sandwich structure are essential for detecting this hormone by selective and ultra-sensitive recognition between antigen and antibody-

immunoassay.[9,84] Nanoparticles, especially those made of noble metals like gold, have special physicochemical features that allow them to be easily integrated into heterogeneous structures and boost biosensing performance.[38,85] The sort of soft-to-soft interactions that were generated between the Au–Zn–Sln-MOF composite and the hCG, or as a result of a coordination bond that was formed with the amino groups in the salen-MOF, represents one of the main ideas of the mechanism of biosensing.[53,86] Due to a decrease in the lipophilicity of the Au–Zn–Sln-MOF composite and an increase in the polarity of the metal ions, the ligand–metal charge transferring (LMCT) effect may be able to support the probability of the chelation process.[87,88] This is because these two factors lead to an increase in the chelation probability.

The color change from yellow to green can be seen by the naked eye when a swab test device is used in conjunction with a colorimetric method based on the formation of sandwich-immunocomplexes between antigen and antibody on the surface of the gold nanoparticles Au–Zn–Sln-MOF@Ab of the highly linked Au–Zn–Sln-MOF composite itself. Additionally, the Au–Zn–Sln-MOF composite acts as an innovative and promising biosensor for direct hCG quantification and monitoring. This is due to the augmentation of the absorbance intensities and the blue shift in the presence of hCG in comparison to other competing analytes.

Experimental

Materials and instrumentation

See the details in (Appendix A: ESI file†).

Procedures

Synthesis of the Au–Zn–Sln-MOF composite. An Au–Zn–Sln-MOF composite is produced by an *in situ* simple reaction of $Zn(NO_3)_2 \cdot 6H_2O$ (2.0 mmol, 0.595 g) and $HAuCl_4 \cdot 3H_2O$ (2.0 mmol, 0.788 g) (Fig. S1†). They were both dissolved in 10 ml of deionized water (DW) and dropped into a round flask containing an organic linker (1.0 mmol) produced by Sheta *et al.*[60] This system was subjected to agitation and refluxing at 100 degrees Celsius for 48 hours. The pale greenish-brown precipitate was filtered, rinsed, and allowed to remain at ambient temperature to dry completely. The overall plan for the reaction is in the ESI file (Fig. S2†).

Preparation and optimization of swab test-based device biosensing platform. In this stage, antibodies to hCG hormone (hCG-Ab) were immobilized on the surface of the Au–Zn–Sln-MOF composite through classic-electrostatic adsorption to create Au–Zn–Sln-MOF@Ab, as described in references with some changes.[20,24,79–81] A 10 M Au–Zn–Sln-MOF composite was suspended in 50 mL of pH 7.4 phosphate buffer solution (PBS). Gradually, the Au–Zn–Sln-MOF composite solution was infused with 2.5 mM of anti-hCG-Ab. At room temperature, in a one-hour incubation period with gentle magnetic stirring, the Au–Zn–Sln-MOF@Ab solution was prepared. After that, the system was left to incubate for an additional hour with 25.0 milliliters (mL) of bovine serum albumin (BSA) containing 1% weight-per-volume bovine serum in order to block the exposed open site on the surface of the Au–Zn–Sln-MOF composite. In order to apply the composition described above to use as a detection probe or biosensing platform (Au–Zn–Sln-MOF@Ab), it was first centrifuged at 4500 rpm for 15 min and then resuspended in 2.5 milliliters of a solution that included 1% PEG 20 000, fructose 2%, sucrose 5%, BSA 1%, Tween-20 0.4%, and trisodium citrate 0.2%) and stored ready for use a CITOSWAB® sterile cotton swab was soaked in a beaker of Au–Zn–Sln-MOF@Ab (25 mL) overnight before being air dried at room temperature. After the swabs had dried, they were ready for use. Therefore, they were examined using both a reference for the hormone hCG and actual samples.

Protocols for the routine colorimetric measurement of hCG hormone. From the 10.0 mL of stock solution (100 mM dissolved in DMSO), a 100.0 mL working solution (10 mM) of the Au–Zn–Sln-MOF composite was made by diluting it with 90 mL of PBS. After that, Au–Zn–Sln-MOF@Ab was formed in the solution using classic-electrostatic conjugation for immobilization. The UV-vis absorbance of the Au–Zn–Sln-MOF@Ab solution was measured and then compared to a freshly generated series of concentrations of the hCG hormone in a buffered solution. The absorbance intensities (Abs) of Au–Zn–Sln-MOF@Ab were found to be linearly related to the hCG hormone concentrations over a range of 0.001 to 3000 mIU mL^{-1} after optimizing the absorption measurement conditions, as shown by the following linear-relationship equation: $Y = a + bX$; "in which Y and X represent the Au–Zn–Sln-MOF@Ab absorption intensities and the hCG hormone concentrations, respectively; a and b represent the intercept and slope of the linear-relationship variations, respectively. Moreover, the LOD and LOQ were calculated "LOD = 3.3SD/b and LOQ = 10SD/b" according to.[89–91] Absorption of the Au–Zn–Sln-MOF@Ab solutions with hCG hormone alone and in a mixture with interfering matrices was assessed for the selectivity investigation.

Quantification of hCG hormone in real samples. The real samples (serum, plasma, or urine) used in this study were handled, pre-treated, and measured as indicated above, all while adhering to the customary procedures established to prevent the spread of infection and according to the ethics protocol mentioned here in a separate section.

Conclusions

A portable swab test equipment is proposed in this study for the qualitative detection of hCG, and a colorimetric method is proposed to determine its quantitative levels. Development by the synthesis of a novel and promising Au–Zn–Sln-MOF utilizing a method that is both straightforward and creatively developed composite using a simple and innovatively devised process forms the basis for the two analytical instruments presented here. Spectroscopic and analytical tools are used to characterize the composites created. In comparison to other published strip devices and publications, the examination of the swab test's statistical validity and technique for measuring color intensity was thorough and appropriate. The swab test gadget is user-friendly, quick, easy, inexpensive, extra-sensitive,

and ultra-selective. It requires no complicated technology, relies on color change, and can be used by anybody in the comfort of their own home. Serum, plasma, and urine tests performed with a cotton swab test instrument may be easily adapted into commercially available, user-friendly kits that are 20–30% less expensive than current market offerings. The biosensor has a detection limit of 0.055 mIU mL^{-1} and a quantification limit of 0.167 mIU mL^{-1}. It displays a fast-stable response for hCG in the range of (0.001–3000 mIU mL^{-1}) under ideal conditions. The designed colorimetric biosensor showed excellent selectivity for hCG compared to the competing matrix. In addition to these benefits, the colorimetric immunoassay approach provided a rapid method for quantifying hCG with reduced limitations of detection and quantification, improved assay speed, and a wider linear detection range.

Ethical statement

The study was conducted in accordance with the Declaration of Helsinki, and approved by the Medical Research Ethics Committee (MREC)—Federal Wide Assurance No. 00014747— at the National Research Centre, Egypt, decision No. 20169, on November 05-2020. In this study, we did not use the samples in any research involving human participants or research involving physical interventions on study participants, or involving processing of personal data but conducted the research according to the method described in the article.

Author contributions

Reda M. Mohamed (RMM), Said M. El-Sheikh (SME-S), Mohammad W. Kadi (MWK), Ammar A. Labib (AAL), Sheta M. Sheta (SMS): conceptualization, SME-S and SMS; methodology, SME-S, AAL and SMS; validation, SME-S and SMS; formal analysis, SME-S, SMS and AAL; investigation, SME-S and SMS; resources, SME-S, SMS and RMM; data curation, SME-S and SMS; writing—original draft preparation, SME-S, and SMS; writing—review and editing, SME-S, SMS, AAL, RMM, and MWK; visualization, SME-S, and SMS; supervision, RMM, and MWK; project administration, RMM, and MWK; funding acquisition, RMM, and MWK. All authors have read and agreed to the published version of the manuscript.

Conflicts of interest

There are no conflicts to declare.

Notes and references

1 V. Van Hoof, D. Barglazan, L. Blairon, B. Braekevelt, R. Debois, N. V. J. De Vos, D. Gruson, J. Jonckheere, K. Lanckmans, M. Moens, B. Peeters, J. Penders, A. Roman, L. Van Hoovels, F. Vanstapel, J. Y. Verbakel, A. Verdonck and A. G. Verstraete, *Acta Clin. Belg.*, 2022, **77**, 329–336.

2 L. Zhao, X. Huang, T. Zhang, X. Zhang, M. Jiang, H. Lu, G. Sui, Y. Zhao, W. Zhao and X. Liu, *J. Pharm. Biomed. Anal.*, 2022, **209**, 114464.

3 Y. Xiao, S. Li, Z. Pang, C. Wan, L. Li, H. Yuan, X. Hong, W. Du, X. Feng, Y. Li, P. Chen and B. F. Liu, *Biosens. Bioelectron.*, 2022, **206**, 114130.

4 S. Mattila, N. Paalanne, M. Honkila, T. Pokka and T. Tapiainen, *JAMA Netw. Open*, 2022, **5**, e2216162.

5 Z. Qu, K. Wang, G. Alfranca, J. M. De Fuente and D. Cui, *Nanoscale Res. Lett.*, 2020, **15**, 10, DOI: **10.1186/s11671-019-3240-3**.

6 S. M. Sheta, A. S. Abdelelmoaty, H. M. Abu Hashish, A. M. Kamel, M. M. Abd-Elzaher and S. M. El-Sheikh, *Anal. Bioanal. Chem.*, 2022, **414**, 8379–8388.

7 F. U. H. Chorionic, *Science*, 2019, 1–8.

8 D. Qin, X. Jiang, G. Mo, X. Zheng and B. Deng, *Microchim. Acta*, 2020, **187**, 482.

9 Z. Zhang, G. Xu, L. Xie and Y. Guan, *Microchim. Acta*, 2019, **186**, 581.

10 F. Tan, F. Yan and H. Ju, *Biosens. Bioelectron.*, 2007, **22**, 2945–2951.

11 Z. Wang, Y. Gao, D. Zhang, Y. Li, L. Luo and Y. Xu, *Arch. Gynecol. Obstet.*, 2020, **301**, 295–302.

12 N. E. Ajubi and N. Nijholt, *Clin. Chem. Lab. Med.*, 2005, **43**, 68–70.

13 L. N. Vuong, T. D. Pham, V. N. A. Ho, T. M. Ho, P. Humaidan and M. Horton, *Front. Endocrinol.*, 2020, **11**, 1–7.

14 D. G. Grenache, *J. Appl. Lab. Med.*, 2020, **9**, 850–857.

15 C. J. Pretorius, S. Toit, U. Wilgen, S. Klingberg, M. Jones, J. P. J. Ungerer and J. R. Tate, *Clin. Chem. Lab. Med.*, 2019, **58**, 438–444.

16 D. G. Grenache, *Clin. Chem. Lab. Med.*, 2020, **58**, 323–325.

17 M. Zygmunt, F. Herr, S. Keller-schoenwetter, C. V Rao, U. W. E. Lang, K. T. Preissner, K. Kunzi-rapp, K. Mu, D. Obstetrics, M. Z. Gynecology, K. T. P. Biochemistry and J. Liebig, *J. Clin. Endocrinol. Metab.*, 2002, **87**, 5290–5296.

18 W. Regelson, *Cancer*, 1195, **76**, 1299–1301.

19 S. Yu, W. Sun, P. Zhang, Y. Chen, L. Yan, L. Geng and D. Yulin, *Chromatographia*, 2020, **83**, 1145–1151.

20 T. Zhang, H. Wang, Z. Zhong, C. Li, W. Chen, B. Liu and Y.-D. Zhao, *Microchem. J.*, 2020, **157**, 105038.

21 J. Camperi, A. Combès, T. Fournier, V. Pichon and N. Delaunay, *Anal. Bioanal. Chem.*, 2020, **412**, 4423–4432.

22 J. Park, H. Jung, Y. Wook, H. Kim, M. Kang and J. Pyun, *Anal. Chim. Acta*, 2015, **853**, 360–367.

23 L. Chen, B. Liu, J. Liu, S. Wan, T. Wu, J. Yuan and S. Member, *IEEE Sens. J.*, 2020, **20**, 9071–9078.

24 Y. Guo, Y. Zhou, S. Xiong, L. Zeng, X. Huang and Y. Leng, *Sens. Actuators, B*, 2020, **305**, 127439.

25 J. Rodrigues, S. O. Pereira, N. F. Santos, C. Rodrigues, F. M. Costa and T. Monteiro, *Appl. Surf. Sci.*, 2020, **527**, 146813.

26 W. Lu, Z.-A. Chen, M. Wei, X. Cao and X. Sun, *Analystst*, 2020, **145**, 8097–8103.

27 M. Roushani and A. Valipour, *Microchim. Acta*, 2016, **183**, 845–853.

28 P. Chen, Q. Sun, F. Xiong, H. Zhong, Z. Yao and Y. Zeng, *Biomicrofluidics*, 2020, **14**, 024107.

29 X. Mao, Y. Ma, A. Zhang, L. Zhang, L. Zeng and G. Liu, *Anal. Chem.*, 2009, **81**, 1660–1668.

30 H. Wang, L. Ma, T. Zhang, K. Huang and Y. Zhao, *Anal. Chim. Acta*, 2020, **1093**, 106–114.

31 A. S. Basaleh and S. M. Sheta, *J. Inorg. Organomet. Polym. Mater.*, 2021, **31**, 1726–1737.

32 A. S. Basaleh and S. M. Sheta, *Anal. Bioanal. Chem.*, 2020, **412**, 3153–3165.

33 M. Gharib, A. Morsali, O. Weingart, C. Janiak and A. Goldman, *Chem. Soc. Rev.*, 2020, 2751–2798.

34 S. M. El-sheikh, D. I. Osman, O. I. Ali, W. Gh, M. A. Shoeib, S. M. Shawky and S. M. Sheta, *Appl. Surf. Sci.*, 2021, **562**, 150202.

35 S. M. Sheta, S. M. El-Sheikh and M. M. Abd-Elzaher, *Dalton Trans.*, 2018, **47**, 4847–4855.

36 J. Liang, A. Nuhnen, S. Millan, H. Breitzke, V. Gvilava, G. Buntkowsky and C. Janiak, *Angew. Chem., Int. Ed.*, 2020, **59**, 6068–6073.

37 S. M. Sheta, S. M. El-Sheikh, M. M. Abd-Elzaher, S. R. Salem, H. A. Moussa, R. M. Mohamed and I. A. Mkhalid, *Appl. Organomet. Chem.*, 2019, **33**, e5249.

38 D. K. Yadav, R. Gupta, V. Ganesan, P. K. Sonkar and M. Yadav, *ChemElectroChem*, 2018, **5**, 2612–2619.

39 M. Müller, S. Turner, O. I. Lebedev, Y. Wang, G. Van Tendeloo and R. A. Fischer, *Eur. J. Inorg. Chem.*, 2011, **5**, 1876–1887.

40 C. Wu, F. Irshad, M. Luo, Y. Zhao and X. Ma, *ChemCatChem*, 2019, **11**, 1256–1263.

41 A. M. Shultz, O. K. Farha, D. Adhikari, A. A. Sarjeant, J. T. Hupp and S. T. Nguyen, *Inorg. Chem.*, 2011, **50**, 3174–3176.

42 A. M. Shultz, A. A. Sarjeant, O. K. Farha, J. T. Hupp and S. T. Nguyen, *J. Am. Chem. Soc.*, 2011, **133**, 13252–13255.

43 A. Bhunia, Y. Lan and A. K. Powell, *Chem. Commun.*, 2011, **47**, 2035–2037.

44 G. Salassa, M. J. J. Coenen, S. J. Wezenberg, B. L. M. Hendriksen, S. Speller, J. A. A. W. Elemans and A. W. Kleij, *J. Am. Chem. Soc.*, 2012, **134**, 7186–7192.

45 L. Leoni and A. D. Cort, *Inorganics*, 2018, **6**, 42.

46 A. K. Asatkar, M. Tripathi and A. Deepali, *Stability and Applications of Coordination Compounds*, 2019, DOI: 10.5772/intechopen.88593.

47 S. Pullen and G. H. Clever, *Acc. Chem. Res.*, 2018, **51**, 3052–3064.

48 R. Wang, L. Wu, B. Chica, L. Gu, G. Xu and Y. Yuan, *J. Mater.*, 2017, **3**, 58–62.

49 K. Leus, Y. Liu, M. Meledina, S. Turner, G. Van Tendeloo and P. Van Der Voort, *J. Catal.*, 2020, **316**, 201–209.

50 S. Go, S. Ernst, E. Hastu, M. Mo, I. El Aita, R. Wiedey, N. Tannert, S. Nießing, S. Abdpour, A. Schmitz, J. Quodbach, G. Fu, S. K. Henninger and C. Janiak, *Ind. Eng. Chem. Res.*, 2019, **58**, 21493–21503.

51 I. Gruber, A. Nuhnen, A. Lerch, S. Nießing, M. Klopotowski, A. Herbst, M. Karg and C. Janiak, *Front. Chem. Rec.*, 2019, 7, 1–19.

52 D. I. Osman, S. M. El-Sheikh, S. M. Sheta, O. I. Ali, A. M. Salem, W. G. Shousha, S. F. EL-Khamisy and S. M. Shawky, *Biosens. Bioelectron.*, 2019, **141**, 111451.

53 S. M. Sheta, S. M. El-sheikh and M. M. Abd-elzaher, *Anal. Bioanal. Chem.*, 2019, **411**, 1339–1349.

54 S. M. Sheta, S. M. El-sheikh, D. I. Osman, A. M. Salem, O. I. Ali, F. A. Harraz, W. G. Shousha, M. A. Shoeib, S. M. Shawky and D. D. Dionysiou, *Dalton Trans.*, 2020, **49**, 8918–8926.

55 A. Tahli, R. F. M. Elshaarawy, Ü. Köc, A. C. Kautz and C. Janiak, *Polyhedron*, 2016, **117**, 579–584.

56 H. B. Tanh Jeazet and C. Janiak, *Encycl. Inorg. Bioinorg. Chem.*, 2014, 403–417.

57 S. M. Sheta, S. M. El-Sheikh, M. M. Abd-Elzaher and A. R. Wassel, *Appl. Organomet. Chem.*, 2019, **33**, e4777.

58 M. Alhaddad and S. M. Sheta, *ACS Omega*, 2020, **5**, 28296–28304.

59 S. M. Sheta, S. M. El-Sheikh and M. M. Abd-Elzaher, *Appl. Organomet. Chem.*, 2019, **33**, e5069.

60 S. M. Sheta, S. M. El-Sheikh, M. M. Abd-Elzaher, M. L. Ghanemc and S. R. Salem, *RSC Adv.*, 2019, **9**, 20463–20471.

61 T. Jun-Qi and S. Q. Man, *Rare Met. Mater. Eng.*, 2013, **42**, 2232–2236.

62 B. I. Pastoriza-santos and L. M. Liz-marza, *Adv. Funct. Mater.*, 2009, **19**, 679–688.

63 I. Pastoriza-santos and L. M. Liz-marza, *Langmuir*, 2002, **18**, 2888–2894.

64 S. Das, A. K. Pandey, A. A. Athawale, M. Subramanian, T. K. Seshagiri, P. K. Khanna and V. K. Manchanda, *J. Hazard. Mater.*, 2011, **186**, 2051–2059.

65 L. Jiang, S. Xu, J. Zhu, J. Zhang, J. Zhu and H. Chen, *Inorg. Chem.*, 2004, **43**, 5877–5883.

66 Z. Zhang, X. Chen, X. Zhang and C. Shi, *Solid State Commun.*, 2006, **139**, 403–405.

67 Y. Isomura, T. Narushima and H. Kawasaki, *Chem. Commun.*, 2012, **48**, 3784–3786.

68 M. Hyotanishi, Y. Isomura, H. Yamamoto and H. Kawasaki, *Chem. Commun.*, 2011, **47**, 5750–5752.

69 H. Yamamoto, H. Yano, H. Kouchi, Y. Obora, R. Arakawa and H. Kawasaki, *Nanoscale*, 2012, **4**, 4148–4154.

70 W. Yao, W. Gong, H. Li and F. Li, *Dalton Trans.*, 2014, **43**, 15752–15759.

71 B. M. Omkaramurthy and G. Krishnamurthy, *Inorg. Nano-Met. Chem.*, 2019, **49**, 375–384.

72 R. Sacourbaravi, Z. Ansari, A. Mohammad, K. Valiollah and N. Esmaeil, *J. Inorg. Organomet. Polym. Mater.*, 2020, **30**, 4615–4621.

73 D. Yin, C. Li, H. Ren, O. Shekhah, J. Liu and C. Liang, *RSC Adv.*, 2017, **7**, 1626–1633.

74 A. Jarrah and S. Farhadi, *RSC Adv.*, 2018, **8**, 37976–37992.

75 A. T. Ezhil Vilian, B. Dinesh, R. Muruganantham, S. R. Choe, S. M. Kang, Y. S. Huh and Y. K. Han, *Microchim. Acta*, 2017, **184**, 4793–4801.

76 N. Kavitha and P. V. A. Lakshmi, *J. Saudi Chem. Soc.*, 2017, **21**, S457–S466.

77 N. Getachew, Y. Chebude, I. Diaz and M. Sanchez-Sanchez, *J. Porous Mater.*, 2014, **21**, 769–773.

78 R. Sacourbaravi, Z. Ansari, A. Mohammad, K. Valiollah and N. Esmaeil, *J. Inorg. Organomet. Polym. Mater.*, 2020, **30**, 4615–4621.

79 J. Ni, R. J. Lipert, G. B. Dawson and M. D. Porter, *Anal. Chem.*, 1999, **71**, 4903–4908.

80 L. Ma, H. Wang, T. Zhang, Y. Xuan, C. Li, W. Chen, B. Liu, B. Chance, B. Photonics, H. Bioinformatics and M. Imaging, *Sens. Actuators, B*, 2019, **298**, 126819.

81 A. Ochratoxin, G. Juice, H. Jiang, X. Li, Y. Xiong, K. Pei, L. Nie and Y. Xiong, *Toxins*, 2017, **9**, 83.

82 **https://www.invitro-test.com/IVD-reagents/immuno-assay/fertility/hCG-Pregnancy-Rapid-Tests.php**, last accessed Jan 1, 2022.

83 **https://www.medicaldisposables.us/hCG-cassette-pregnancy-test-p/w1-c.htm.last**, accessed Jan 1, 2022.

84 X. Luo, J. J. Davis and J. J. Davis, *Chem. Soc. Rev.*, 2013, **42**, 5944–5962.

85 Z. Ye, L. Wei and L. Xiao, *Chem. Sci.*, 2019, **10**, 5793–5800.

86 L. Zhang, J. Wang, T. Du, W. Zhang, W. Zhu, C. Yang, T. Yue, J. Sun, T. Li and J. Wang, *Inorg. Chem.*, 2019, **58**, 12573–12581.

87 S. Pal, A. Bhunia, P. P. Jana, S. Dey, J. Möllmer, C. Janiak and H. P. Nayek, *Chem.–Eur. J.*, 2015, **21**, 2789–2792.

88 Y. Wu, W. Wu, L. Zou, J. Feng, C. Gu, B. Li, S. R. Batten, R. Yadav and A. Kumar, *Inorg. Chem. Commun.*, 2016, **70**, 160–163.

89 M. M. Abd-Elzaher, M. A. Ahmed, A. B. Farag, M. Attia, A. O. Youssef and S. M. Sheta, *Egypt. J. Chem.*, 2016, **59**, 701–718.

90 M. M. Abd-Elzaher, M. A. Ahmed, A. B. Farag, M. S. Attia, A. O. Youssef and S. M. Sheta, *Sens. Lett.*, 2017, **15**, 977–981.

91 S. M. Sheta, M. A. Akl, E. Saad and E. R. H. El-gharkawy, *RSC Adv.*, 2020, **10**, 5853–5863.